Research Square

Preprints are preliminary reports that have not undergone peer review.
They should not be considered conclusive, used to inform clinical practice,
or referenced by the media as validated information.

Label-free Optical Metabolic Imaging Differentiates Breast Cancer Cells based on Receptor Status

Xinyu Li
University of Arkansas
Alan Woessner
University of Arkansas
Meichen Liu
University of Arkansas
Timothy Muldoon
University of Arkansas
Narasimhan Rajaram
University of Arkansas
Chenguang Fan
cf021@uark.edu
University of Arkansas

Research Article

Keywords:

Posted Date: November 27th, 2026

DOI: https://doi.org/10.21203/rs.3.rs-11680017/v1

License: This work is licensed under a Creative Commons Attribution 4.0 International License.
Read Full License

Additional Declarations: No competing interests reported.

Label-free Optical Metabolic Imaging Differentiates Breast Cancer Cells based on Receptor Status

Xinyu Li[1], Alan Woessner[2], Meichen Liu[2], Timothy Muldoon[1,2], Narasimhan Rajaram[1,2], Chenguang Fan* [1,3]

[1]Cell and Molecular Biology Program, University of Arkansas, Fayetteville, AR 72701, USA
[2]Department of Biomedical Engineering, University of Arkansas, Fayetteville, AR 72701, USA
[3]Department of Chemistry and Biochemistry, University of Arkansas, Fayetteville, AR 72701, USA
*Correspondence: cf021@uark.edu

Abstract

Cellular metabolism becomes an emerging biomarker to determine breast cancer subtypes and stages. Optical metabolic imaging utilizes the endogenous fluorescence of nicotinamide adenine dinucleotide (NADH), its phosphorylated form (NADPH), and flavin adenine (FAD) to evaluate cellular metabolism in a non-invasive and quantitative manner. In this study, we applied two-photon excited fluorescence microscopy to determine the optical redox ratio, NAD(P)H bound fraction, and mitochondrial fractal dimension of 26 human breast cancer cell lines from six distinct subtypes. We found significant differences in the optical redox ratio, NAD(P)H bound fraction, and mitochondrial fractal dimension. The combination of these three optical metabolic parameters was able to differentiate breast cell lines based on their subtypes. The dependency of these three optical metabolic parameters on breast cancer receptor status were also investigated. This study provides both functional and structural information of metabolic variations in a large panel of human breast cancer cell lines from different subtypes.

Introduction

Breast cancer is the most common cancers in women, accounting for ~30% of all new female cancers annually. According to American Cancer Society, the probability of one woman to develop breast cancer during lifetime is approximately 13% (1 in 8). The overall 5-year relative survival rate for breast cancer is ~90% but with a much lower rate (33%) for the metastatic stage. Thus, early diagnosis of breast cancer is essential for making corresponding treatment plans. Currently, the treatment for breast cancer mainly depends on the receptors identified in patients, mostly including estrogen receptor (ER) and human epidermal growth factor receptor 2 (HER2). However, only ~60% ER+ patients can respond to ER-inhibitors such as tamoxifen, while ~30% of HER2+ patients do not respond to HER2-inhibitors such as trastuzumab[1,2]. Thus, additional biomarkers to fast determine breast cancer properties and responses to therapy are necessary.

Cancer cells commonly have reprogrammed metabolism for their rapid growth and metastasis[3]. The well-known Warburg effect states that even with sufficient oxygen supply, cancer cells tend to use glycolysis rather than oxidative phosphorylation to generate energy and intermediate compounds to meet their growth needs[4]. This phenomenon, so called aerobic glycolysis, has also been found in breast cancer cells[5,6]. Breast cancer receptors ER and HER2 have been shown to enhance aerobic glycolysis by facilitating glucose transport and activating glycolysis[7-9]. Thus, cellular metabolism truly reflects changes in cancer cell properties regarding different cell types and stages.

Nicotinamide adenine dinucleotide (NAD^+/NADH), its phosphorylated form ($NADP^+$/NADPH), and flavin adenine dinucleotide (FAD/$FADH_2$) are essential electron-carrier coenzymes for energy production or biosynthesis. The ratio of these coenzymes reflects dynamic changes in cellular metabolism. Because of the similar fluorescence feature, NADH and NADPH are referred to as NAD(P)H in this study. NAD(P)H and FAD have endogenous fluorescence, so the measurement of their autofluorescence by optical imaging offers a label-free and non-invasive approach to evaluate and monitor cellular metabolism[10-12]. Specifically for breast cancer research, the optical redox ratio (defined as FAD/[NAD(P)H+ FAD] in this study) has been used to differentiate receptor status, identify metastatic changes, and monitor treatment responses[13-17]. In addition to the redox ratio, optical imaging can also measure the time of a fluorescent molecule in the excited state by fluorescence lifetime imaging (FLIM), which depends on free or bound states of the molecule. Free NAD(P)H has a short lifetime, while protein-bound NAD(P)H has a long lifetime[18]. This approach has also been used as an indicator for cellular metabolism in breast cancer[17,19,20].

Recently, mitochondrial fractal dimension quantified by optical microscopy has become an emerging biomarker to evaluate cellular energy production during cancer development[21-23]. The fractal describes an object with self-similar structures at different scales, and the fractal dimension is a measurement of such property. Mitochondrial organization follows fractal properties and undergoes changes by fusion or fission depending on metabolic needs[24,25]. Because of the high concentrations of NAD(P)H and FAD in the mitochondria, mitochondrial organization can be evaluated by their endogenous fluorescence signals[26]. A combination of multiple optical parameters - redox ratio, fluorescence lifetime, and mitochondrial organization - has been shown to be more reliable for mapping metabolic changes compared with using a single optical parameter [27-29].

Over the years, researchers have identified multiple subtypes of breast cancer. However, comprehensive metabolic profiling of these different subtypes using optical imaging has been lacking. In this study, we applied optical metabolic imaging to determine the redox ratio, NAD(P)H bound fraction, and mitochondrial fractal dimension of 26 representative cell lines from the ATCC breast cancer cell panel that are commonly used for breast cancer research (Table 1), providing both functional and structural information related to breast cancer cell metabolism in a non-invasive and quantitative manner.

Table 1. Cell lines tested in this study

Cell line	Subtype*	ER status**	PR status	HER2 status
Hs578Bst	Normal	–	–	–
MCF10A	Normal	–	–	–
MCF12A	Normal	–	–	– or low
HMEC	Normal	low	low	low
MCF7	Luminal A	+	+	–
MDA-MB-134-VI	Luminal A	+	–	–
HCC1500	Luminal A	+	+	–
HCC1428	Luminal A	+	+	–
BT474	Luminal B	+	+	+
MDA-MB-361	Luminal B	+	+	+
ZR-75-30	Luminal B	+	–	+
UACC812	Luminal B	+	–	+
AU565	HER2 positive	–	–	+
MDA-MB-453	HER2 positive	–	–	+

HCC1954	HER2 positive	–	–	+
HCC202	HER2 positive	–	–	+
UACC893	HER2 positive	–	–	+
HCC1937	Triple negative A	–	–	–
MDA-MB-468	Triple negative A	–	–	–
HCC1143	Triple negative A	–	–	–
HCC70	Triple negative A	–	–	–
BT549	Triple negative B	–	–	–
HCC1395	Triple negative B	–	–	–
Hs578T	Triple negative B	–	–	–
MDA-MB-157	Triple negative B	–	–	–
HCC38	Triple negative B	–	–	–

* Cell line subtypes were determined based on previous literatures[30,31].
* ER, PR, HER2 statuses were determined based on previous literatures[32,33].

Results

Optical redox ratios of breast cancer cell subtypes

Each cell line listed in Table 1 was imaged with three biological replicates, and 5 images were captured for each replicate. The normal cell group had a lower NAD(P)H intensity than all subtypes of breast cancer cells tested in this study, while the NAD(P)H intensity in ER+ or HER2+ cells was higher than triple-negative breast cancer (TNBC) cells (Figure 1A).

The optical redox ratio in this study was calculated by the equation of FAD/[NAD(P)H+FAD)], which has a range of 0 to 1 with a typically normal distribution[29] (Figure 1A). To remove pixels within cells that are not of interest besides nuclei, cytoplasmic pixels with high autofluorescence intensities in the red emission channel at 855nm excitation were omitted when calculating the redox ratio (refer to description in the Methods section). The optical redox ratio had a V-shaped pattern with increased cell aggressiveness from non-cancerous to TNBC (Figure 1B). The group of normal cells had the highest optical redox ratio, while the luminal B (LB) subtype with both ER and HER2 expressed had the lowest optical redox ratio.

One-Way ANOVA and Tukey's HSD tests were performed to compare the optical redox ratios among different cell subtypes (Figure 1C). The normal group had a significantly higher redox ratio than all breast cancer subtypes ($p<0.001$), consistent with previous optical imaging studies[14,15]. Luminal breast cancer cell lines are characterized by ER+ with or without PR expression. According to HER2 status, luminal cell lines can be further grouped into two subtypes, luminal A (LA, ER+/HER2-) and luminal B (LB, ER+/HER2+)[30,31]. LB cell lines are typically more invasive and aggressive than LA cell lines[34]. The optical redox ratio was significantly different between LA

and LB subtypes tested in this study ($p<0.001$), consistent with previous optical imaging studies[15,17]. The optical redox ratios of LB and HER2+ subtypes were significantly lower than normal cells and other breast cancer cell subtypes ($p<0.001$). Being the most heterogeneous, TNBC cell lines can also be further categorized into two subtypes. Triple-negative A (TNA) cell lines are enriched with basal markers, while triple-negative B (TNB) cell lines overexpress genes related to tumor invasiveness and aggressiveness, exhibiting more mesenchymal-like features[35]. Our results showed that the TNA subtype had a significantly lower optical redox ratio than the TNB subtype ($p<0.001$), which is consistent with the previous optical imaging study on TNBC[16]. Although most groups had significantly different optical redox ratios from other subtypes, the optical redox ratios were not significantly different between LA and both TNBC subtypes ($p=0.0572$ and 0.4239, respectively), indicating that the optical redox ratio alone could not differentiate breast cancer cell subtypes perfectly in this study.

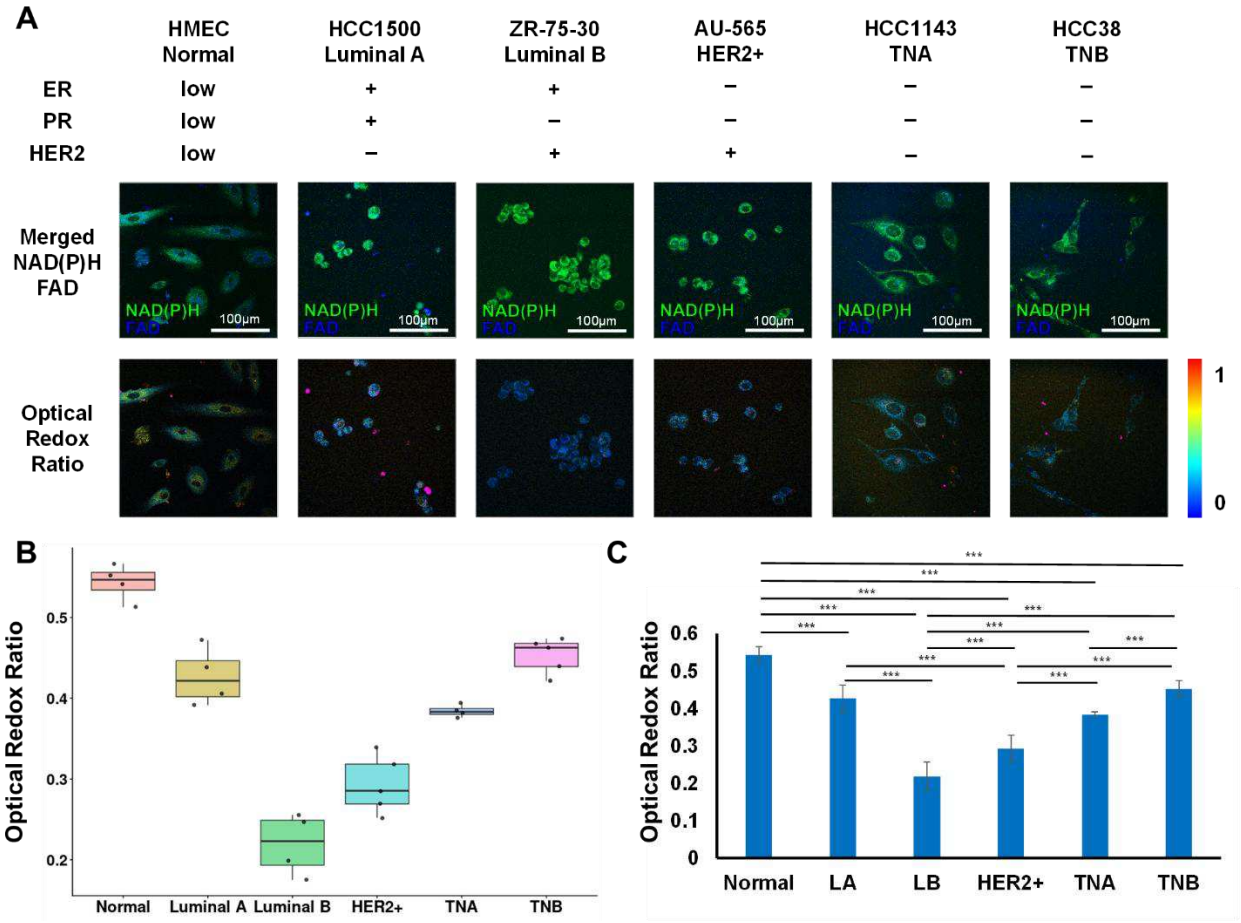

Figure 1. The optical redox ratios of breast cancer cell subtypes. A) Optical images of representative breast cancer cell lines. One representative cell line for each group was shown. All images of each cell line were provided as supplementary information. The upper panels are merged NAD(P)H and FAD images, and the lower panels are optical redox ratio images [FAD/(NAD(P)H+FAD)]. Pink regions corresponding to relatively high autofluorescence signals in the red emission channel were omitted for calculation. B) The

box plot of the optical redox ratio for each group. The mean values of each cell line (n=3) were plotted as individual points. C) The values (mean ± SEM) of the optical redox ratio for each group. The mean values of each cell line within one group were used to calculate significant difference between groups. ***: $p<0.001$.

FLIM of breast cancer cell subtypes

Next, we used FLIM to determine the mean NAD(P)H lifetime and the fractions of free and bound NAD(P)H in cells, which are correlated by the equation $\tau_m = A1\tau_1 + A2\tau_2$ (τ_m: mean fluorescence lifetime; τ_1: short lifetime; τ_2: long lifetime; A1: free fraction; A2: bound fraction) (Figure 2A). The NAD(P)H bound fraction directly indicates the NAD(P)H state in cells, so we compared the NAD(P)H bound fraction A2 (from 0 to 1) in different cell subtypes, which had an inverted V-shaped pattern with increased cell aggressiveness (Figure 2B). It increased in ER+ or HER2+ cells, reaching the maximum in the HER2+ subtype, and then decreased in TNBC cells. Such trend was also observed in a previous imaging study on breast cancer cells[17].

One-Way ANOVA and Tukey's HSD tests were performed to compare the NAD(P)H bound fraction among different cell subtypes (Figure 2C). The normal group was significantly lower than all breast cancer subtypes ($p=0.0018$ for TNB and $p<0.001$ for all other subtypes). The HER2+ group had a significantly higher NAD(P)H bound fraction than all other cell subtypes ($p<0.001$). The two subtypes of TNBC were also significantly different from each other ($p<0.001$). The two subtypes of luminal cell lines (LA and LB) were significantly different ($p<0.001$), but both were not significantly different from the TNA subtype ($p=0.2192$ and 0.0708, respectively). Thus, the NAD(P)H bound fraction alone could not differentiate breast cancer cell subtypes perfectly in this study either.

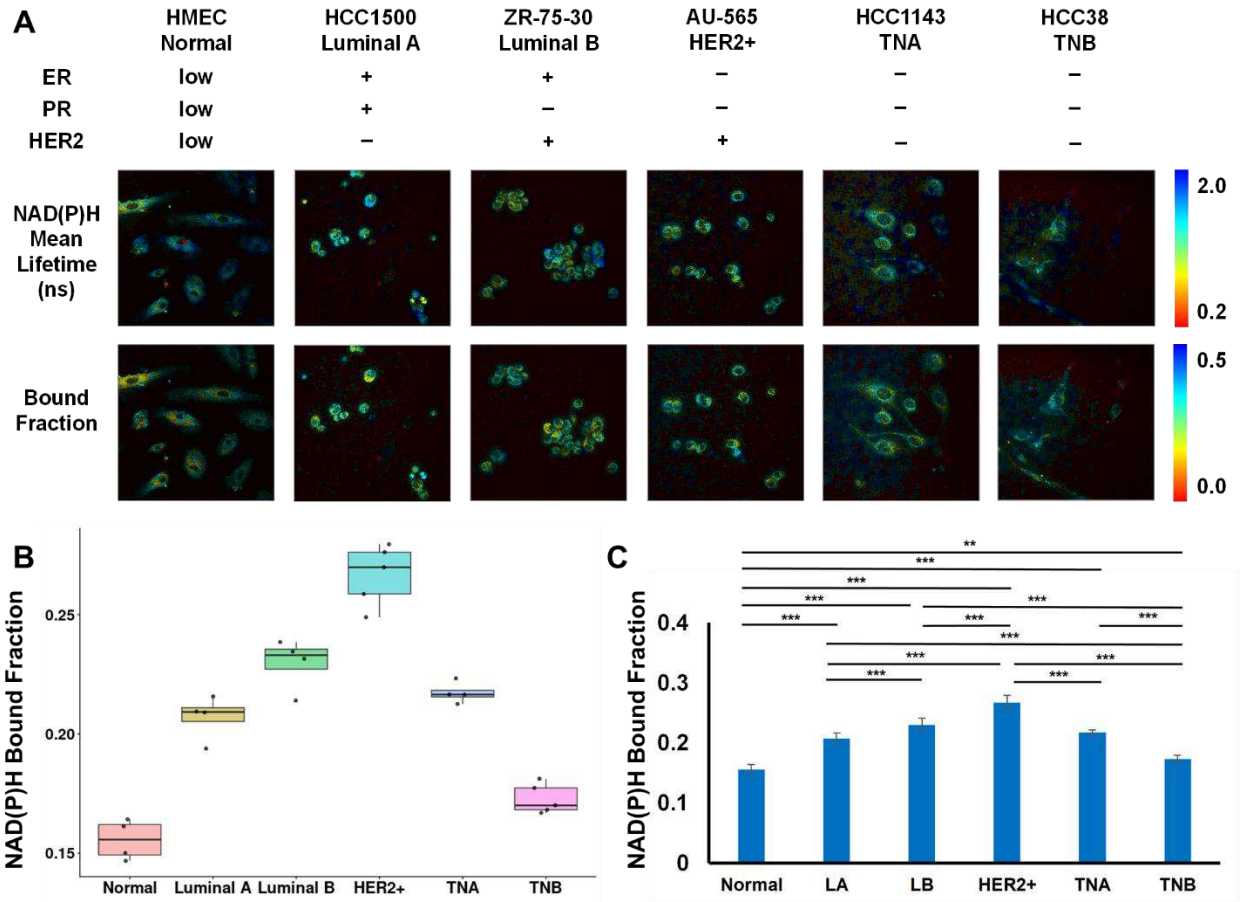

Figure 2. FLIM of breast cancer cell subtypes. A) FLIM images of representative breast cancer cell lines. One representative cell line for each group was shown. All images of each cell line were provided as supplementary information. The upper panels are NAD(P)H mean lifetimes (τ_m), and the lower panels are NAD(P)H bound fractions (A2). $\tau_m = A1\tau_1 + A2\tau_2$ (τ_1: short lifetime; τ_2: long lifetime; A1: free fraction). B) The box plot of the NAD(P)H bound fraction for each group. The mean values of each cell line (n=3) were plotted as individual points. C) The values (mean ± SEM) of the NAD(P)H bound fraction for each group. The mean values of each cell line within one group were used to calculate significant difference between groups. **: $p<0.01$; ***: $p<0.001$.

Mitochondrial fractal dimension of breast cancer cell subtypes

Finally, we determined the mitochondrial fractal dimension of each breast cancer cell subtype by optical imaging (Figure 3A). Generally, a lower fractal dimension means the loss of structural complexity and indicates a more fragmented structural resulting from a higher fission/fusion ratio, while a higher fractal dimension shows a higher structural complexity and interconnected network, which is commonly observed in normal cells[36]. In this study, the mitochondrial fractal dimension in cells had an approximately V-shaped pattern with increased cell aggressiveness (Figure 3B). The group of normal cells had the highest fractal dimension value, while the HER2+ subtype had the lowest fractal dimension value.

One-Way ANOVA and Tukey's HSD tests were performed to compare the fractal dimension among different breast cancer cell subtypes (Figure 3C). The normal group, the HER2+, and the TNB subtypes had significantly different fractal dimension from all other cell subtypes tested in this study ($p<0.01$ or $p<0.001$). However, both subtypes of luminal cell lines and the TNA group could not be differentiated from each other by mitochondrial fractal dimension ($p=0.9752$, 0.7464, and 0.9892, respectively). Thus, the differentiation of breast cancer cell subtypes by mitochondrial fractal dimension is not as good as the redox ratio and FLIM shown above.

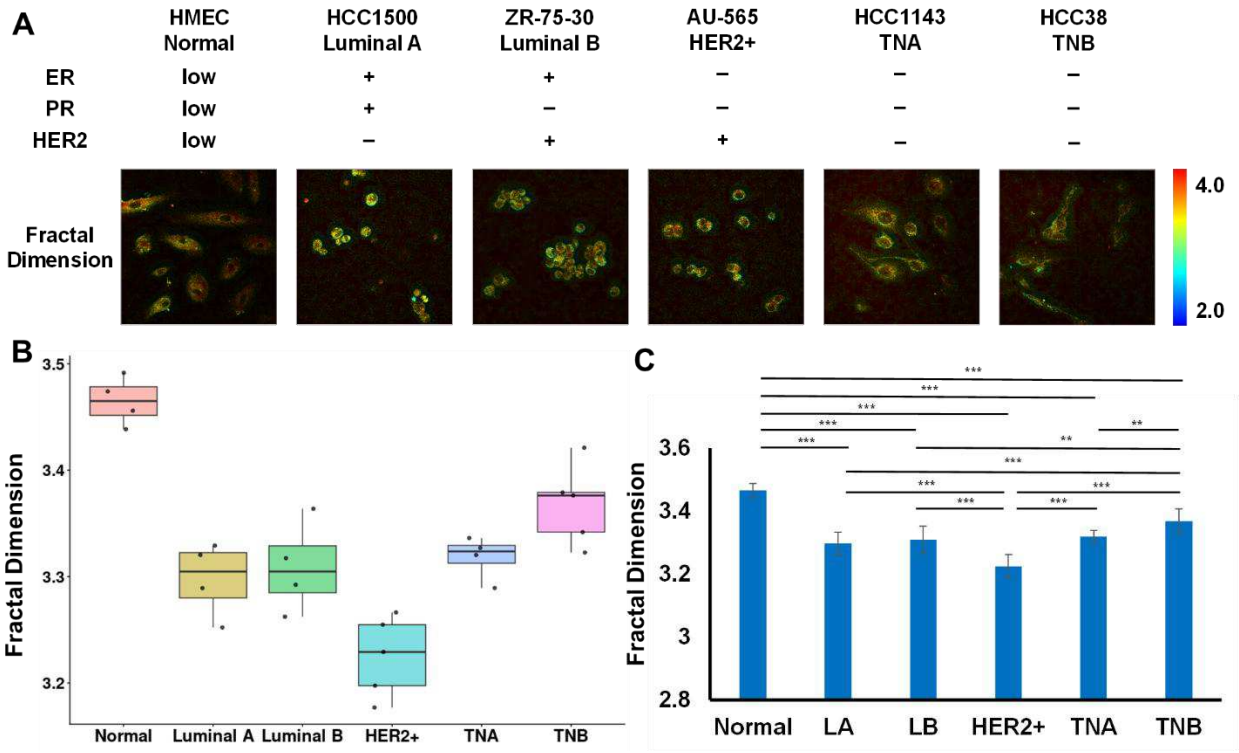

Figure 3. Fractal dimension of breast cancer cell subtypes. A) Fractal dimension images of representative breast cancer cell lines. One representative cell line for each group was shown. All images of each cell line were provided as supplementary information. B) The box plot of the fractal dimension for each group. The mean values of each cell line (n=3) were plotted as individual points. C) The values (mean ± SEM) of the fractal dimension for each group. The mean values of each cell line within one group were used to calculate significant difference between groups. **: $p<0.01$; ***: $p<0.001$.

Discussion

Differentiation of breast cancer cell subtypes by optical metabolic imaging

In this study, we applied optical metabolic imaging to monitor metabolism changes temporally and spatially in a large panel of breast cancer cells with 4 or 5 representative cell lines in each subtype (Table 1). While other studies have examined a combination of the optical redox ratio,

fluorescence lifetime, and mitochondrial organization in various biological specimens, this is the first comprehensive study on cancer cell lines to report all three metrics and the correlations between them. Our results indicated that none of the optical redox ratio, NAD(P)H bound fraction, or mitochondrial fractal dimension could perfectly differentiate breast cancer cell subtypes alone. The optical redox ratio could not separate the LA subtype from TNBC; The NAD(P)H bound fraction and mitochondrial fractal dimension could not differentiate the TNA subtype from luminal cell lines. Thus, we aimed to combine two or three optical imaging readouts to differentiate breast cancer cell subtypes. The mean values of the three metrics for each cell line were plotted in a 2D or 3D scatterplot (Figure 4).

The use of two metabolic imaging parameters allows efficient separation of the breast cancer subtypes. In all three 2D scatterplots, the normal and the HER2+ subtypes are well separated from all other cell subtypes. In the 2D scatterplot of the redox ratio and NAD(P)H bound fraction, there is no overlap among any other cell subtypes, though TNA and LA subtypes are relatively close to each other (Figure 4A). For the other two 2D scatterplots, there are overlaps among either the LA subtype and both TNBC subtypes or the TNA subtype and both luminal cell subtypes (Figure 4B and 4C). Thus, the combination of the redox ratio and NAD(P)H bound fraction could differentiate breast cancer cell subtypes better than using only one optical imaging readout. A combination of all three parameters was also able to separate different cell subtypes well (Figure 4D). A previous imaging study showed that the combination of NAD(P)H mean lifetime and the redox ratio could differentiate breast cancer cells with different molecular subtypes (normal, luminal, HER2+, and TNBC)[17]; however, this study examined a limited number of cell lines (1 cell line/subtype). In our study, we investigated a larger panel of breast cancer cell lines with 4 or 5 representative cell lines in each subtype to provide solid evidence that optical imaging can indeed distinguish breast cancer cell subtypes. Furthermore, our results also demonstrated such separation even in the additional subtypes of luminal (LA and LB) and TNBC (TNA and TNB) cells.

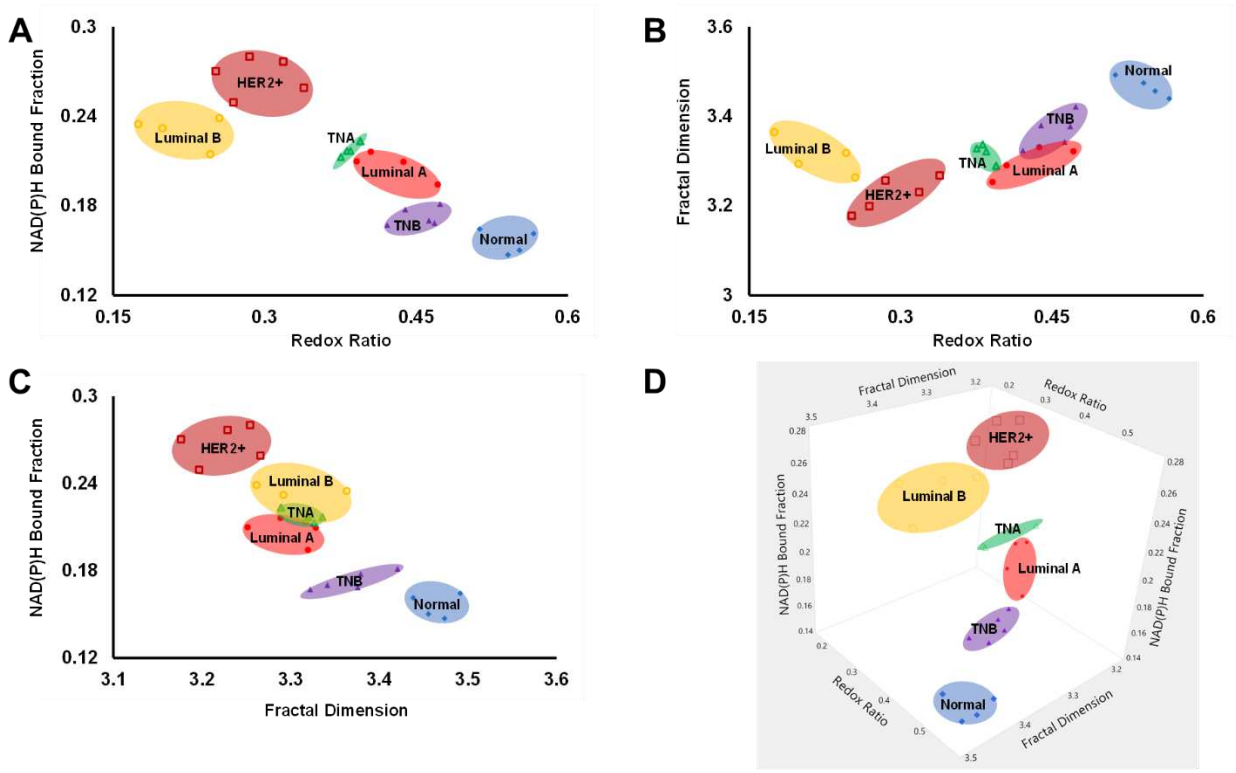

Figure 4. Differentiation of breast cancer cell subtypes by optical imaging. A) The 2D scatterplot of the redox ratio and NAD(P)H bound fraction for each cell line. B) The 2D scatterplot of the redox ratio and mitochondrial fractal dimension for each cell line. C) The 2D scatterplot of mitochondrial fractal dimension and NAD(P)H bound fraction for each cell line. D) The 3D scatterplot of the redox ratio, NAD(P)H bound fraction, and mitochondrial fractal dimension for each cell line. The mean values of each cell line (n=3) were plotted. The 3D scatterplot was generated by JMP. Normal cells: blue solid diamond; LA: red solid cycle; LB: yellow ring; HER2+: red square; TNA: green triangle; TNB: purple solid triangle.

The dependence of optical imaging metrics on ER status

Approximately 80% of invasive breast cancers are ER+[37]. Estrogens and ERs have been well known for their roles in regulating glucose transport, glycolysis, citric acid cycle, and oxidative phosphorylation[38-41], thus affecting optical imaging outcomes. Indeed, a previous imaging study has shown that the optical redox ratio could differentiate breast cancer cell lines based on ER status[14]. Thus, we aimed to determine whether optical imaging readouts besides the redox ratio also depend on ER status with a larger number of breast cancer cell lines tested in this study.

The values of the three optical imaging metrics of the ER- group (normal, HER2+, TNA, and TNB) and the ER+ group (LA and LB) were tested by unpaired *t*-tests (Figure 5). Consistent with the previous study, the redox ratio of the ER+ group was significantly lower than that of the ER- group ($p=0.0499$). However, the other two metrics were not significantly different between ER+ and ER- groups ($p=0.4308$ for the NAD(P)H bound fraction, $p=0.3138$ for the mitochondrial fractal dimension).

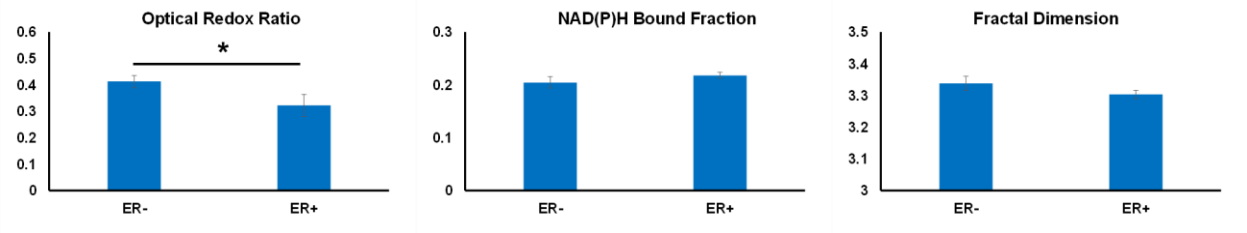

Figure 5. The dependence of optical imaging metrics on ER status. The values (mean ± SEM) of optical imaging metrics for ER- (normal, HER2+, TNA, and TNB) and ER+ (LA and LB) groups. n=3 for each cell line. *: p<0.05.

The dependence of optical imaging metrics on HER2 status

Approximately 15% to 20% of all breast cancer cases are HER2+[37]. HER2+ cells commonly have reprogramed metabolism with upregulated glycolysis by activating signaling pathways such as PI3K/AKT and MAPK, enhanced lipid production for membrane synthesis, and increased glutamine uptake for fueling the TCA cycle[42-44]. A previous imaging study has demonstrated that the redox ratio was decreased in HER2 overexpressing breast cancer cells[15]. Thus, we aimed to determine whether optical imaging metrics besides the redox ratio also depend on HER2 status with a larger number of breast cancer cell lines tested in this study.

The values of the three optical imaging metrics of the HER2- group (normal, LA, TNA, and TNB) and the HER2+ group (LB and HER2+) were tested by unpaired *t*-tests (Figure 6). Interestingly, all three optical imaging metrics were significantly different between HER2+ and HER2- groups, ($p<0.001$ for the redox ratio, $p<0.001$ for the NAD(P)H bound fraction, and $p=0.0043$ for the mitochondrial fractal dimension). Consistent with the previous study, the HER2+ group had a significantly lower redox ratio than that of the HER2- group[15]. Moreover, the HER2+ group had a significantly higher NAD(P)H bound fraction and lower fractal dimension than those of the HER2- group. These results demonstrate that changes in HER2 status have a greater effect on optical metabolic imaging parameters that ER status.

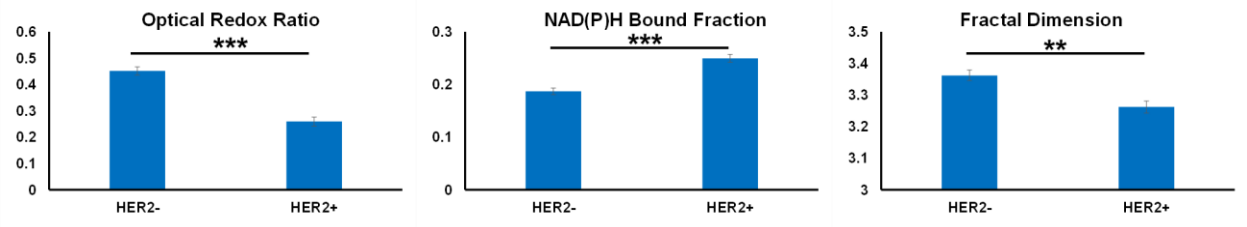

Figure 6. The dependence of optical imaging metrics on HER2 status. The values (mean ± SEM) of optical imaging metrics for HER2- (normal, LA, TNA, and TNB) and HER2+ (LB and HER2+) groups. n=3 for each cell line. **: p<0.01. ***: p<0.001.

The dependence of optical imaging metrics on PR status

Approximately 65% of all breast cancer cases are PR+. The majority of PR+ breast cancer are also ER+, making ER+/PR+ the most abundant subtype of breast cancer[37]. The expression of PR depends on estrogen[45], while PR can suppress ERα action in breast cancer[46]. To date, there has been no study on the association of optical imaging results with PR status. Thus, we aimed to determine whether optical imaging metrics depend on PR status in this study.

The values of the three optical imaging metrics of the PR+ group (MCF7, HCC1500, HCC1428, BT474, MDA-MB-361) and the PR- group (all the other 21 cell lines tested in this study) were tested by unpaired *t*-tests (Figure 7A). None of three metrics were significantly different between PR+ and PR- groups (p=0.2708 for the redox ratio, p=0.1677 for the NAD(P)H bound fraction, p=0.4696 for the mitochondrial fractal dimension), which could result from the dependency of PR expression on ER status.

ER-/PR+ breast cancer is rare, and there were no ER-/PR+ cell lines tested in this study. Therefore, we determined whether optical imaging metrics depend on PR status in ER+ cells. The values of the three optical imaging metrics of the ER+/PR+ group (MCF7, HCC1500, HCC1428, BT474, MDA-MB-361) and the ER+/PR- group (MDA-MB-134-VI, ZR-75-30, UACC812) were tested by unpaired *t*-tests (Figure 7B). The redox ratio was significantly higher in ER+/PR+ cells than that in ER+/PR- cells (p=0.0068 for the redox ratio, p=0.0905 for the NAD(P)H bound fraction, p=0.9545 for the mitochondrial fractal dimension). This is consistent with the finding that PR can suppress ERα action in breast cancer[46], while ER overexpression decreases redox ratios[14]. Thus, the redox ratio could differentiate breast cancer cells depending on PR status only in ER+ cells.

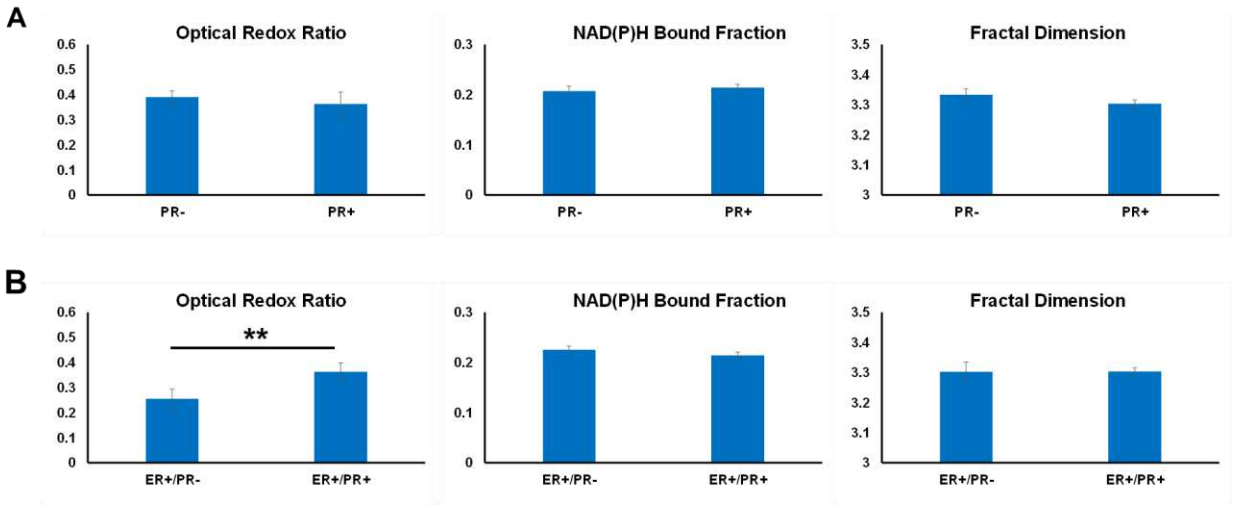

Figure 7. The dependence of optical imaging metrics on PR status. A) The values (mean ± SEM) of optical imaging metrics for PR- and PR+ groups. n=3 for each cell line. B) The values (mean ± SEM) of optical imaging metrics for ER+/PR- and ER+/PR+ groups. n=3 for each cell line. **: p<0.01.

The correlation between optical imaging metrics in breast cancer cells

As shown above, the three optical imaging metrics tested in this study (the redox ratio, NAD(P)H bound fraction, and mitochondrial fractal dimension) had various patterns in different breast cancer cell subtypes and varied dependencies on the receptor status. Thus, we aimed to determine whether these three metrics are mutually independent or correlated with each other in breast cancer cells. The mean values of the three optical imaging readouts for each cell line were plotted in a 2D scatterplot (Figure 4). All three metrics were strongly correlated with each other. The NAD(P)H bound fraction decreased with an increase in the redox ratio, while the mitochondrial fractal dimension demonstrated a strong positive correlation with the redox ratio. As a result, the fractal dimension was also negative correlated with the NADH bound fraction.

Previous work has shown a strong correlation between the redox ratio and the glycolytic index (the ratio of moles of glucose consumed to moles of lactate produced) in breast cancer cells[17]. Our data were well aligned with these previous results. ER+ or HER2+ cells have a higher glycolytic level[47,48], leading to an increased NADH intensity and a decreased redox ratio (Figures 5 & 6). PR+ cells have a lower ER level, so the redox ratio was increased in ER+/PR+ cells compared to ER+/PR- cells (Figure 7B).

While we determined both the mean NADH lifetime and the protein-bound NADH fraction, we have focused on the NADH bound fraction for investigating the effects of receptor status, differences between subtypes and correlations between metabolic parameters. Sharick *et al.* have shown that amongst all fluorescence lifetime parameters, the NAD(P)H bound fraction alone is sensitive to the different metabolic pathways along which glucose is directed[49]. The general consensus in is that the optical redox ratio (as defined here) and the mean NAD(P)H lifetime (and hence protein-bound NAD(P)H lifetime) move in the same direction, with a few exceptions[17,28,50]. Cells engaged in increased glycolysis generate more free cytosolic NADH, which is expected to lead to a decrease in the optical redox ratio, NADH bound fraction as well as the mean NADH lifetime (free NADH has a shorter lifetime than bound NADH)[29]. However, in our study, we observed that lower redox ratios were associated with higher fractions of protein-bound NADH. Indeed, our results showed that the redox ratio is negatively correlated with the NAD(P)H bound fraction ($r = -0.817$, $p < 0.001$). The higher protein-bound NADH fraction can likely be explained by the binding of NADH to lactate dehydrogenase during the catabolism of glucose to lactate, which can increase protein-bound NADH lifetime and contribution[50]. Generation of NADPH through the pentose phosphate pathway for biosynthesis can also lead to a decrease in the redox ratio. FLIM outcomes depend on not only metabolic pathways but also many other factors, including the distribution of NAD(P)H-binding enzymes, changes in dynamic quenching, and

mitochondrial pH levels[28,51]. Nevertheless, our study here on 26 different breast cancer cell lines appears to present data contradictory to conventional assumptions about the fluorescence lifetime. The correlation between the redox ratio and FLIM readouts should be carefully considered on a case-by-case manner depending on cell types and growth stages, and they should be used together to precisely determine metabolic changes in cells.

Mitochondrial fractal dimension measures the complexity of mitochondrial structures and networks in cells. Healthy cells commonly have a higher mitochondrial fractal dimension and a balanced mitochondrial fusion and fission[52]. On the other hand, mitochondria in cancer cells tend to break apart into more fragmented structures to adapt to reprogramed metabolism, thus lowering mitochondrial fractal dimension[53]. Indeed, our results showed that cells in the normal group had the highest mitochondrial fractal dimension, while the HER2+ breast cancer subtype had the lowest mitochondrial fractal dimension (Figure 3). Moreover, we demonstrated that the mitochondrial fractal dimension of cell lines tested in this study depended on HER2 status (Figure 6). The correlation between mitochondrial fractal dimension and the redox ratio is highly positive ($r = 0.719$, $p < 0.001$), consistent with previous studies which showed that increased catabolism of glucose (decreasing redox ratio) is commonly associated with mitochondria fission (lowering fractal dimension)[54,55]. However, as one optical imaging readout alone, mitochondrial fractal dimension has no strong dependence on ER or PR status as well as a clear separation of breast cancer cell subtypes. Thus, it should be used in combination with other biomarkers such as the redox ratio to evaluate the metabolic changes in cancer cells.

In summary, we tested a large panel of totally 26 representative breast cancer cell lines in this study, providing strong evidence that optical metabolic imaging can differentiate breast cancer cell subtypes by combining two or three different optical metabolic parameters. By providing both functional and structural information of metabolic variations in different breast cancer cell subtypes, we showed the correlation between optical metabolic imaging metrics. To the best of our knowledge, this is the first comprehensive study to integrate the redox ratio, FLIM, and mitochondrial fractal dimension for a large panel of breast cancer cells and the first to study the dependency of optical metabolic imaging parameters on PR status in breast cancer.

Methods

Cell culture

All cell lines were purchased from the American Type Culture Collection (ATCC). All cell lines were cultured with corresponding protocols provided by ATCC. Specifically, cell lines HCC1500, HCC1428, ZR7530, AU565, HCC1954, HCC202, HCC1937, HCC1143, HCC70, HCC1395 and

HCC38 were cultured in ATCC-formulated RPMI-1640 Medium (ATCC 30-2001) with 10% fetal bovine serum (FBS) (ATCC 30-2020). BT549 was cultured in RPMI-1640 Medium with 10% FBS and 0.023U/mL human insulin (Sigma-Aldrich 11061-68-0). Hs578T was cultured in Dulbecco's Modified Eagle's Medium (DMEM, ATCC 30-2002) with 10% FBS and 0.01mg/mL human insulin. MCF7 was cultured in ATCC-formulated Eagle's Minimum Essential Medium (EMEM, ATCC 30-2003) with 10% FBS and 0.01mg/ml human insulin. Primary human mammary epithelial cells (HMEC) were cultured in Mammary Epithelial Cell Basal Medium (ATCC PCS-600-030) and Mammary Epithelial Cell Growth Kit (ATCC PCS-600-040). MCF10A and MCF12A was cultured in Mammary Epithelial Cell Growth Medium (MEGM, Lonza CC-3150) and 100ng/ml cholera toxin (MilliporeSigma C8052). BT474 was culture in ATCC Hybri-Care Medium (ATCC 46-X) with 10% FBS. Hs578Bst was cultured in ATCC Hybri-Care Medium with 10% FBS and 30ng/mL human epidermal growth factor (hEGF, ThermoFisher AF-100-15). All above cells were maintained at 37°C incubator with 5% CO_2. The other cell lines MDA-MB-157, MDA-MB-453, MDA-MB-468 and UACC893 were cultured in ATCC-formulated Leibovitz's L-15 Medium (ATCC 30-2008) supplemented with 10% FBS. MDA-MB-361 and MDA-MB-134-VI were also cultured in ATCC-formulated Leibovitz's L-15 Medium but with 20% FBS. UACC812 was cultured in Leibovitz's L-15 medium with 20% FBS and 2mM L-glutamine and 20ng/mL hEGF. All these cell lines were maintained at 37°C with 100% air without CO_2. All cells were used within the first 10 passages for all experiments. For cell imaging experiments, each cell line was grown to a density of ~10^5 cells per 35mm glass-bottom imaging dish (MatTek P35G-1.5-14-C) with at least three biological replicates.

Multiphoton microscopy

To collect cellular autofluorescence of NADH and FAD, multiphoton microscopy was used. A laser scanning multiphoton microscope (Ultima Investigator+, Bruker) coupled with an ultrafast pulsed laser (InsightX3; Spectra-physics) was used to induce two-photon excited fluorescence (TPEF) and collect fluorescence intensity and fluorescence lifetime. The ultrafast laser has a laser repetition rate of 80MHz, and all images were collected while the microscope was in an inverted configuration. Laser pulses were focused on glass bottom dishes containing cultured cells using a 25x (1.1NA) water immersion objective (N25X-APO-MP, Nikon). To maintain cell viability during imaging, cell dishes were incubated at 37°C, and 5% CO_2 at 100% humidity using a micro-incubation setup (DH-40IL, Warner Instruments). For each culture dish, the microscope was set to have a consistent laser dwell time of 0.6μs, and the measured power at the objective was maintained at approximately 10-15mW. For each culture dish, 7 random fields-of-view were

chosen for image collection. Additionally, 32 frame averaging was used to reduce background noise, and an optical zoom of 2 was used. Each collected image was 512 x 512 pixels large, with a spatial resolution of 0.524μm / pixel.

The microscope was equipped with 4 fluorescence emission wavelength channels that were collected simultaneously: 637 ± 32.5nm (red), 525 ± 25nm (green), 460 ± 20nm (blue), and >440nm (UV). NADH autofluorescence was collected at a fluorescence excitation wavelength of 755nm and a fluorescence emission wavelength of 460nm. FAD autofluorescence was collected at a fluorescence excitation wavelength of 855nm, and a fluorescence emission wavelength of 525nm. These excitation/emission channels are specifically chosen such that NADH and FAD autofluorescence signals were optically isolated. Along with NADH autofluorescence, NADH fluorescence lifetime was also collected using an additional Time Tagger (Time Tagger Ultra; Swabian) module at the same excitation/emission band as NADH autofluorescence. To ensure a high signal-to-noise ratio, a photon flux of >1E5 photon counts/s was maintained, and an integration time of 60s was used during collection of fluorescence lifetime measurements.

Analysis of TPEF images

Quantitative analysis of NADH and FAD autofluorescence was performed in a stepwise fashion using custom MATLAB code. Firstly, fluorescence intensity images were normalized to relative μM concentrations of fluorescein based on previously established calibration methods. Briefly, these methods use the known relationship between collected fluorescence intensity image, laser power measured at the objective, and PMT detector gain to estimate the concentration of fluorescein at each pixel of the image[24].

Next, cell-positive masks were generated which highlight the location of cell-positive pixels within each image. To generate these masks, the pretrained Cellpose2[56] neural network was implemented, by utilizing the ‘cellpose’ and ‘segmentCells2D’ functions within MATLAB. Since cells appeared in culture as either single cells or cell clusters, two separate “ImageCellDiameter” values were used: 20 pixels for single cells and 80 pixels for cell clumps. These values were chosen via visual confirmation between the cell-positive mask and the intensity image. Once both masks were generated, they were combined to create a final cell-positive mask that encompassed all cells within an image.

To further remove pixels within cells that are not of interest, specifically nuclei, the average from all fluorescein normalized excitation and emission channels (8 total) was calculated, then the averaged image was blurred using a small gaussian filter (3x3 pixel window, σ = 0.5) and a threshold of 0.04μM fluorescein was applied. This concentration-based threshold effectively removed all nuclei-positive pixels while preserving NADH and FAD containing pixels within cells. Interestingly, at 855nm excitation, the red fluorescence emission channel also showed small cytoplasmic features that exhibited high fluorescence intensity, whose fluorescence also shown brightly in the green FAD emission channel. Since this red channel fluorescence is not indicative of FAD autofluorescence, and would greatly impact the optical redox ratio, the red channel was used to remove pixels within the cells that had a high red fluorescence intensity. To achieve this, the red emission channel at 855nm excitation was first blurred using the same small gaussian filter as before, and a concentration threshold of 0.1 was applied. Finally, pixels were only considered for further analysis if they were cell-positive, had an average intensity >0.04μM fluorescein, and an 855nm excitation/ red channel emission ≤0.1μM fluorescein.

The optical redox ratio (ORR), which is a ratio of FAD to NADH raging between 0 and 1 was calculated as

$$ORR = \frac{FAD}{NADH+FAD} \quad (1)$$

To reduce the effect of noise within the normalized NADH and FAD images when calculating the optical redox ratio, the average NADH and FAD values were calculated from all pixels that met the cellular and intensity-based conditions described above[12]. Although not used for statistical comparisons, a pixelwise map of optical redox ratio was also calculated and pseudo-colored for visualization of the redox ratio.

Along with measurements of optical redox ratio, the mitochondrial clustering was also quantified within cells via the mitochondrial fractal dimension. This was done using a previously established modified blanket method, which performs textural analysis on the NADH autofluorescence intensity image and calculates the local fractal dimension based on a defined disk-shaped pixel window surrounding each pixel in the image[23]. For this dataset, a disk-shaped window with a radius of 19 pixels was used, which was based on the average size of single cells within the collected images. Once pixelwise maps of local fractal dimension were calculated, the average fractal dimension was calculated from all pixels that met the cellular and intensity-based

conditions described above. Maps of local fractal dimension were also pseudo-colored for visualization.

Analysis of FLIM images

NADH fluorescence lifetime is a complementary autofluorescence measurement that allows for unmixing of free NADH (0.3-0.4ns lifetime) and protein-bound NADH (3-5ns lifetime). Along with the optical redox ratio, the relative percentage of protein-bound NADH allows for a better understanding of cellular metabolism[29]. All fluorescence lifetime decays are assumed to fit a bi-exponential decay model,

$$S(t) = A_1 e^{-\frac{t}{\tau_1}} + A_2 e^{-\frac{t}{\tau_2}}$$

where A_1 and τ_1 are the relative contribution and lifetime of free NADH, and A_2 and τ_2 are the relative contribution and lifetime of protein-bound NADH, respectively. At the time of acquisition, the lifetime signal is convoluted with an equipment-specific instrument response function (IRF). The IRF for the system used was measured via second harmonic generation (SHG) of a beta-barium borate (BBO) crystal. Deconvolution of the IRF and bi-exponential decay fitting were performed using commercial software (SPCImage, Becker-Hickl), where the quality of model fitting was determined by optimizing fit parameters to ensure a X_2^r close to 1. Following pixel-wise fitting, the proportion of protein-bound NADH was calculated as

$$A_2\% = \frac{A_2}{A_1 + A_2}$$

such that $A_1 + A_2 = 1$. Using the same valid cellular mask as the optical redox ratio quantification, the average $A_2\%$ was computed using the average A_1 and A_2.

Statistical analysis

Each cell line had three biological replicates (n=3), and each replicate had 5 images captured (field of view). For comparison within multiple groups, each field of view was nested within each replicate for the same cell line, and nested analysis of variance (ANOVA) with Turkey's post hoc tests were performed using R software. For comparison between two groups, two-tailed unpaired *t*-tests were performed using R software. The significant level was set as 0.05. Other information such as sample sizes and p values were provided in the main text or figure legends.

Author contributions

XL, AW performed experiments; XL, AW, ML, TM, CF analyzed data; XL, AW, NR, CF wrote the manuscript; All authors edited the manuscript.

Consent for publication

All authors have read and approved the final version of the manuscript and consent to its publication.

Ethics approval and consent to participate

This article does not contain any studies with human participants or animals performed by any of the authors.

Funding

This work was supported by the National Institute of General Medical Sciences under the awards P20GM139768 and R15GM159279, and the Arkansas Integrative Metabolic Research Center at the University of Arkansas. The content is solely the responsibility of the authors and does not necessarily represent the official views of the National Institutes of Health.

Competing interests

The authors declare no competing interests.

Data availability

All data generated or analyzed during this study are included in this published article and its supplementary information files.

Supplementary Information

File S1. The optical images of all breast cancer cell lines.

Reference

1 Chang, J. *et al.* Prediction of clinical outcome from primary tamoxifen by expression of biologic markers in breast cancer patients. *Clin Cancer Res* **6**, 616-621 (2000).

2 Vogel, C. L. *et al.* Efficacy and safety of trastuzumab as a single agent in first-line treatment of HER2-overexpressing metastatic breast cancer. *J Clin Oncol* **20**, 719-726, doi:10.1200/JCO.2002.20.3.719 (2002).

3 Ohshima, K. & Morii, E. Metabolic Reprogramming of Cancer Cells during Tumor Progression and Metastasis. *Metabolites* **11**, doi:10.3390/metabo11010028 (2021).

4 Warburg, O., Wind, F. & Negelein, E. The Metabolism of Tumors in the Body. *J Gen Physiol* **8**, 519-530, doi:10.1085/jgp.8.6.519 (1927).

5 Wu, Z., Wu, J., Zhao, Q., Fu, S. & Jin, J. Emerging roles of aerobic glycolysis in breast cancer. *Clin Transl Oncol* **22**, 631-646, doi:10.1007/s12094-019-02187-8 (2020).

6 Shin, E. & Koo, J. S. Glucose Metabolism and Glucose Transporters in Breast Cancer. *Front Cell Dev Biol* **9**, 728759, doi:10.3389/fcell.2021.728759 (2021).

7 Kocdor, M. A. *et al.* Progressive increase of glucose transporter-3 (GLUT-3) expression in estrogen-induced breast carcinogenesis. *Clin Transl Oncol* **15**, 55-64, doi:10.1007/s12094-012-0882-3 (2013).

8 Imbert-Fernandez, Y. *et al.* Estradiol stimulates glucose metabolism via 6-phosphofructo-2-kinase (PFKFB3). *J Biol Chem* **289**, 9440-9448, doi:10.1074/jbc.M113.529990 (2014).

9 Holloway, R. W. & Marignani, P. A. Targeting mTOR and Glycolysis in HER2-Positive Breast Cancer. *Cancers (Basel)* **13**, doi:10.3390/cancers13122922 (2021).

10 Chance, B., Cohen, P., Jobsis, F. & Schoener, B. Intracellular oxidation-reduction states in vivo. *Science* **137**, 499-508, doi:10.1126/science.137.3529.499 (1962).

11 Georgakoudi, I. & Quinn, K. P. Label-Free Optical Metabolic Imaging in Cells and Tissues. *Annu Rev Biomed Eng* **25**, 413-443, doi:10.1146/annurev-bioeng-071516-044730 (2023).

12 Georgakoudi, I. *et al.* Consensus guidelines for cellular label-free optical metabolic imaging: ensuring accuracy and reproducibility in metabolic profiling. *J Biomed Opt* **30**, doi:10.1117/1.Jbo.30.S2.S23901 (2025).

13 Alhallak, K., Rebello, L. G., Muldoon, T. J., Quinn, K. P. & Rajaram, N. Optical redox ratio identifies metastatic potential-dependent changes in breast cancer cell metabolism. *Biomed Opt Express* **7**, 4364-4374, doi:10.1364/BOE.7.004364 (2016).

14 Ostrander, J. H. *et al.* Optical redox ratio differentiates breast cancer cell lines based on estrogen receptor status. *Cancer Res* **70**, 4759-4766, doi:10.1158/0008-5472.CAN-09-2572 (2010).

15 Walsh, A., Cook, R. S., Rexer, B., Arteaga, C. L. & Skala, M. C. Optical imaging of metabolism in HER2 overexpressing breast cancer cells. *Biomed Opt Express* **3**, 75-85, doi:10.1364/BOE.3.000075 (2012).

16 Jiang, J., Feng, M., Jacob, A., Li, L. Z. & Xu, H. N. Optical Redox Imaging Differentiates Triple-Negative Breast Cancer Subtypes. *Adv Exp Med Biol* **1269**, 253-258, doi:10.1007/978-3-030-48238-1_40 (2021).

17 Walsh, A. J. *et al.* Optical metabolic imaging identifies glycolytic levels, subtypes, and early-treatment response in breast cancer. *Cancer Res* **73**, 6164-6174, doi:10.1158/0008-5472.CAN-13-0527 (2013).

18 Lakowicz, J. R., Szmacinski, H., Nowaczyk, K. & Johnson, M. L. Fluorescence lifetime imaging of free and protein-bound NADH. *Proc Natl Acad Sci U S A* **89**, 1271-1275, doi:10.1073/pnas.89.4.1271 (1992).

19 Plekhanov, A. A. *et al.* The Study of Metabolic Characteristics of Breast Cancer Metastases Using Fluorescence Lifetime Imaging Microscopy. *Biochemistry (Mosc)* **90**, 1397-1408, doi:10.1134/S0006297925603491 (2025).

20 Karrobi, K. *et al.* Fluorescence Lifetime Imaging Microscopy (FLIM) reveals spatial-metabolic changes in 3D breast cancer spheroids. *Sci Rep* **13**, 3624, doi:10.1038/s41598-023-30403-7 (2023).

21 Xylas, J. *et al.* Noninvasive assessment of mitochondrial organization in three-dimensional tissues reveals changes associated with cancer development. *Int J Cancer* **136**, 322-332, doi:10.1002/ijc.28992 (2015).

22 Levitt, J. M. *et al.* Diagnostic cellular organization features extracted from autofluorescence images. *Opt Lett* **32**, 3305-3307, doi:10.1364/ol.32.003305 (2007).

23 Vargas, I. *et al.* Rapid quantification of mitochondrial fractal dimension in individual cells. *Biomed Opt Express* **9**, 5269-5279, doi:10.1364/BOE.9.005269 (2018).

24 Quinn, K. P. *et al.* Quantitative metabolic imaging using endogenous fluorescence to detect stem cell differentiation. *Sci Rep* **3**, 3432, doi:10.1038/srep03432 (2013).

25 Pouli, D. *et al.* Imaging mitochondrial dynamics in human skin reveals depth-dependent hypoxia and malignant potential for diagnosis. *Sci Transl Med* **8**, 367ra169, doi:10.1126/scitranslmed.aag2202 (2016).

26 Xylas, J., Quinn, K. P., Hunter, M. & Georgakoudi, I. Improved Fourier-based characterization of intracellular fractal features. *Opt Express* **20**, 23442-23455, doi:10.1364/OE.20.023442 (2012).

27 Walsh, A. J. *et al.* Quantitative optical imaging of primary tumor organoid metabolism predicts drug response in breast cancer. *Cancer Res* **74**, 5184-5194, doi:10.1158/0008-5472.CAN-14-0663 (2014).

28 Liu, Z. *et al.* Mapping metabolic changes by noninvasive, multiparametric, high-resolution imaging using endogenous contrast. *Sci Adv* **4**, eaap9302, doi:10.1126/sciadv.aap9302 (2018).

29 Kolenc, O. I. & Quinn, K. P. Evaluating Cell Metabolism Through Autofluorescence Imaging of NAD(P)H and FAD. *Antioxid Redox Signal* **30**, 875-889, doi:10.1089/ars.2017.7451 (2019).

30 Dai, X., Cheng, H., Bai, Z. & Li, J. Breast Cancer Cell Line Classification and Its Relevance with Breast Tumor Subtyping. *J Cancer* **8**, 3131-3141, doi:10.7150/jca.18457 (2017).

31 Witt, B. L. & Tollefsbol, T. O. Molecular, Cellular, and Technical Aspects of Breast Cancer Cell Lines as a Foundational Tool in Cancer Research. *Life (Basel)* **13**, doi:10.3390/life13122311 (2023).

32 Kao, J. *et al.* Molecular profiling of breast cancer cell lines defines relevant tumor models and provides a resource for cancer gene discovery. *PLoS One* **4**, e6146, doi:10.1371/journal.pone.0006146 (2009).

33 Neve, R. M. *et al.* A collection of breast cancer cell lines for the study of functionally distinct cancer subtypes. *Cancer Cell* **10**, 515-527, doi:10.1016/j.ccr.2006.10.008 (2006).

34 Creighton, C. J. The molecular profile of luminal B breast cancer. *Biologics* **6**, 289-297, doi:10.2147/BTT.S29923 (2012).

35 Prat, A. *et al.* Molecular characterization of basal-like and non-basal-like triple-negative breast cancer. *Oncologist* **18**, 123-133, doi:10.1634/theoncologist.2012-0397 (2013).

36 Zamponi, N. *et al.* Mitochondrial network complexity emerges from fission/fusion dynamics. *Sci Rep* **8**, 363, doi:10.1038/s41598-017-18351-5 (2018).

37 Anderson, W. F., Katki, H. A. & Rosenberg, P. S. Incidence of breast cancer in the United States: current and future trends. *J Natl Cancer Inst* **103**, 1397-1402, doi:10.1093/jnci/djr257 (2011).

38 Cheng, C. M., Cohen, M., Wang, J. & Bondy, C. A. Estrogen augments glucose transporter and IGF1 expression in primate cerebral cortex. *FASEB J* **15**, 907-915, doi:10.1096/fj.00-0398com (2001).

39 Cai, Q., Lin, T., Kamarajugadda, S. & Lu, J. Regulation of glycolysis and the Warburg effect by estrogen-related receptors. *Oncogene* **32**, 2079-2086, doi:10.1038/onc.2012.221 (2013).

40 Chen, J. Q., Brown, T. R. & Russo, J. Regulation of energy metabolism pathways by estrogens and estrogenic chemicals and potential implications in obesity associated with increased exposure to endocrine disruptors. *Biochim Biophys Acta* **1793**, 1128-1143, doi:10.1016/j.bbamcr.2009.03.009 (2009).

41 Chen, J. Q., Yager, J. D. & Russo, J. Regulation of mitochondrial respiratory chain structure and function by estrogens/estrogen receptors and potential physiological/pathophysiological implications. *Biochim Biophys Acta* **1746**, 1-17, doi:10.1016/j.bbamcr.2005.08.001 (2005).

42 Raghav, K. P. S. & Moasser, M. M. Molecular Pathways and Mechanisms of HER2 in Cancer Therapy. *Clin Cancer Res* **29**, 2351-2361, doi:10.1158/1078-0432.CCR-22-0283 (2023).

43 Cheng, X. A Comprehensive Review of HER2 in Cancer Biology and Therapeutics. *Genes (Basel)* **15**, doi:10.3390/genes15070903 (2024).

44 Exman, P. & Tolaney, S. M. HER2-positive metastatic breast cancer: a comprehensive review. *Clin Adv Hematol Oncol* **19**, 40-50 (2021).

45 Li, Z., Wei, H., Li, S., Wu, P. & Mao, X. The Role of Progesterone Receptors in Breast Cancer. *Drug Des Devel Ther* **16**, 305-314, doi:10.2147/DDDT.S336643 (2022).

46 Mohammed, H. *et al.* Progesterone receptor modulates ERalpha action in breast cancer. *Nature* **523**, 313-317, doi:10.1038/nature14583 (2015).

47 Lu, Z. X. *et al.* CUEDC1 promotes glycolytic metabolism reprogramming through the CUEDC1/CACNG4/PI3K axis to promote ER-positive breast cancer growth. *Cell Mol Biol Lett* **30**, doi:10.1186/s11658-025-00819-2 (2025).

48 Yuan, J. Q., Wang, S. M. & Guo, L. S100A9 promotes glycolytic activity in HER2-positive breast cancer to induce immunosuppression in the tumour microenvironment. *Heliyon* **9**, doi:10.1016/j.heliyon.2023.e13294 (2023).

49 Sharick, J. T. *et al.* Protein-bound NAD(P) H Lifetime is Sensitive to Multiple Fates of Glucose Carbon. *Sci Rep-Uk* **8**, doi:10.1038/s41598-018-23691-x (2018).

50 Zhou, H. *et al.* Non-invasive Optical Biomarkers Distinguish and Track the Metabolic Status of Single Hematopoietic Stem Cells. *iScience* **23**, 100831, doi:10.1016/j.isci.2020.100831 (2020).

51 Yu, Q. & Heikal, A. A. Two-photon autofluorescence dynamics imaging reveals sensitivity of intracellular NADH concentration and conformation to cell physiology at the single-cell level. *J Photochem Photobiol B* **95**, 46-57, doi:10.1016/j.jphotobiol.2008.12.010 (2009).

52 Adebayo, M., Singh, S., Singh, A. P. & Dasgupta, S. Mitochondrial fusion and fission: The fine-tune balance for cellular homeostasis. *FASEB J* **35**, e21620, doi:10.1096/fj.202100067R (2021).

53 Awad, A. & Abdul Karim, N. Dysregulation of Mitochondrial Function in Cancer Cells. *Int J Mol Sci* **26**, doi:10.3390/ijms26146750 (2025).

54 Sun, X. *et al.* Mitochondrial fission produces a Warburg effect via the oxidative inhibition of prolyl hydroxylase domain-2. *Redox Biol* **81**, 103529, doi:10.1016/j.redox.2025.103529 (2025).

55 Guido, C. *et al.* Mitochondrial fission induces glycolytic reprogramming in cancer-associated myofibroblasts, driving stromal lactate production, and early tumor growth. *Oncotarget* **3**, 798-810, doi:10.18632/oncotarget.574 (2012).

56 Pachitariu, M. & Stringer, C. Cellpose 2.0: how to train your own model. *Nature methods* **19**, 1634-1641, doi:10.1038/s41592-022-01663-4 (2022).

Supplementary Files

This is a list of supplementary files associated with this preprint. Click to download.

- SOMallimages.pdf